The Physics of the Unconfined Deflagration-to-Detonation Transition

A.Y. Poludnenko,[1] V.N. Gamezo,[1] and E.S. Oran[2]
[1]*Laboratories for Computational Physics and Fluid Dynamics*
[2]*Materials Science and Component Technology Directorate*

Introduction: Since the discovery of the detonation phenomenon in the late 19th Century, the question of the physical processes that produce these supersonic reaction waves has been at the forefront of combustion science. Due to the extremely large destructive potential of detonations, understanding the mechanisms of their formation so as to prevent them is crucial for the safety of fuel storage facilities, chemical plants, and the like. On the other hand, the ability to initiate detonations in a controlled and efficient manner promises to revolutionize energy-generation and propulsion systems for the Navy through the introduction of detonation-based engines.

Detonations are also studied for the key role they play in a very different type of explosion, those occurring on astronomical scales and known as Type Ia supernovae (SNIa). These are thermonuclear incinerations of compact, white dwarf stars comprised primarily of carbon and oxygen. While the precise mechanism of SNIa is still uncertain, virtually all observationally viable explosion scenarios today involve the formation of a detonation during the later stages of the explosion.

The unifying aspect of all such systems is that burning typically starts as a highly subsonic flame. In order for a detonation to appear, some mechanism must increase pressure dramatically and produce strong shocks. Both experimental and numerical studies over the past several decades have shown that expansion of hot gases in semiconfined systems, e.g., in channels or pipes, can produce fast supersonic flows capable of generating shocks. In the interior of a star or a fuel-vapor cloud, however, there are no walls to confine the flow or to create boundary layers that can generate turbulence and accelerate burning. Is the formation of a detonation from a subsonic flame, known as the deflagration-to-detonation transition (DDT), even possible in such unconfined systems? What mechanisms could produce the pressure increase necessary for DDT?

Modeling Unconfined DDT: In order for pressure to rise in the system, burning needs to accelerate to speeds that are a significant fraction of the speed of sound. Laminar chemical and thermonuclear flames are typically much slower than that. In unconfined systems, the agent capable of providing necessary acceleration is turbulence, which stretches and wrinkles the flame, thus increasing its surface area and the effective burning rate. Typically, this turbulence is the result of the explosion itself. For instance, in SNIa, hot, light, burning products rising through the interior of a star result in the Rayleigh–Taylor instability, which produces strong turbulence.

Modern computational resources do not allow us to study the entire explosion self-consistently in a numerical simulation, since it would require resolving both the smallest scales of burning, namely, the flame thickness, as well as the largest scales, on which turbulence is generated. These scales are typically separated by many orders of magnitude over the range from millimeters to hundreds of meters on Earth or thousands of kilometers in SNIa.

We, therefore, adopted a different approach, in which only a small section of a much larger turbulent flame is modeled in a simulation.[1,2] Homogeneous, isotropic turbulence is steadily driven in a long rectangular domain. This reproduces the effect of the turbulent cascade from much larger scales, which are not included in the calculations. To maximize the range of scales that can be resolved, we use simplified single-reaction chemical kinetics, which is calibrated to represent H_2–air or CH_4–air mixtures. This also allows for the comparison with the experiments.

Interaction of fast turbulence with the flame leads to the development of the highly complex structure shown in Fig. 1. A systematic survey of a large parameter space of turbulent intensities and system sizes demonstrated that, in sufficiently large systems, such fast turbulent flames are susceptible to the spontaneous development of a detonation.[3] This process does not require any confining effect of walls or the presence of external boundaries or obstacles. It is an inherent property of turbulent reacting flows not present in their nonreacting counterparts.

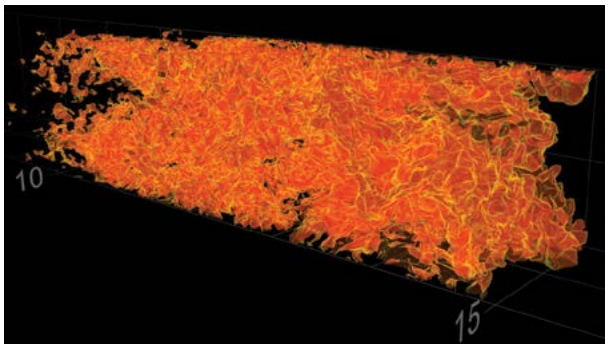

FIGURE 1
Complex structure of the turbulent chemical flame in a stoichiometric methane–air mixture. Uniform computational grid has dimensions 1.33 × 1.33 × 42.5 cm and resolution of ~50 μm. Shown is the isosurface of the fuel mass fraction corresponding to peak reaction rate. In this simulation, burning is fully resolved on all scales. Image rendering by the Department of Defense HPCMP Data Analysis and Assessment Center.

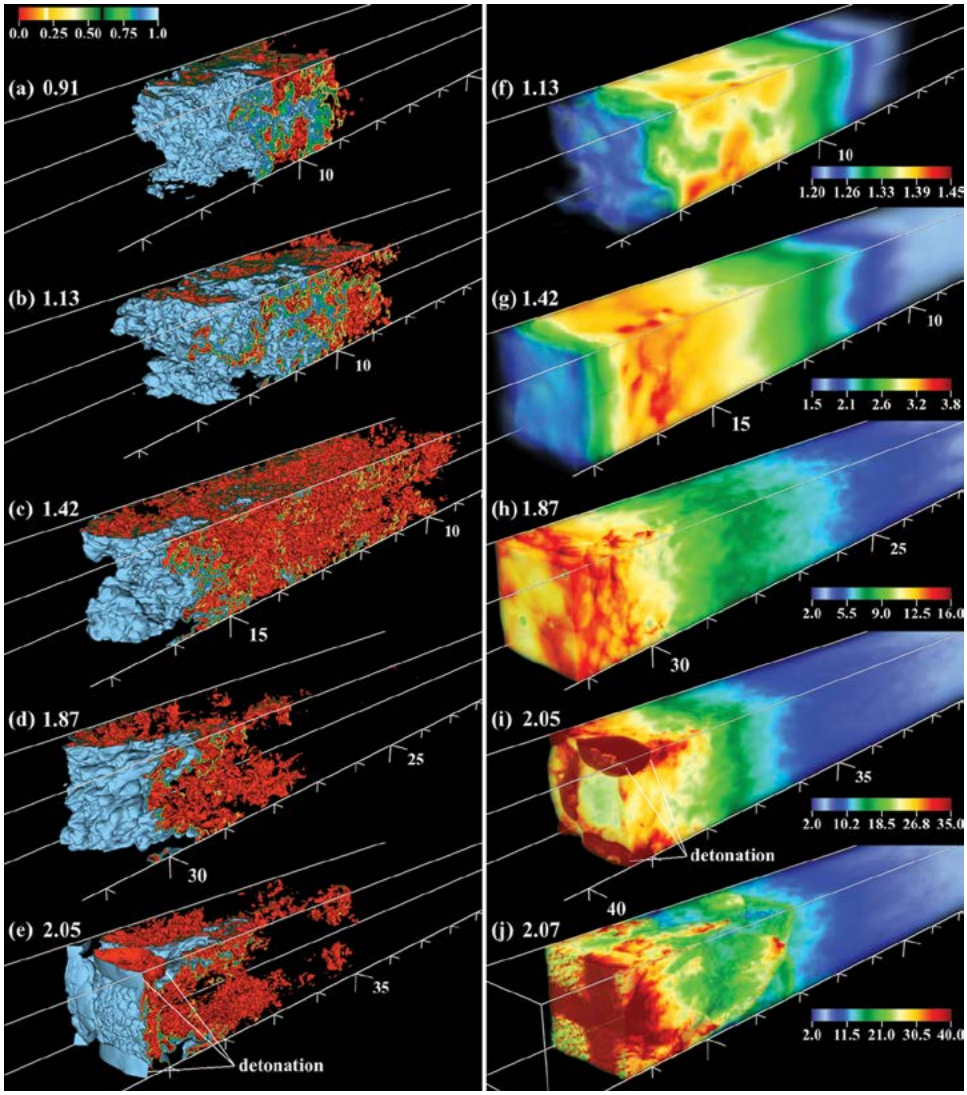

FIGURE 2
Structure of the turbulent flame and the corresponding pressure distribution during DDT in a stoichiometric CH_4–air mixture. (a) – (e): isovolume of the fuel mass fraction. (f) – (j): volume rendering of pressure normalized by the initial pressure in the domain (note a different colormap range in each panel). Horizontal axis scale gives the distance from the right boundary of the domain in centimeters. The time from the start of the simulation is indicated in each panel in units of the large-scale turbulent eddy turnover time. Note that panels (b)-(f), (c)-(g), (d)-(h), (e)-(i) correspond to the same time instants.

Illustration of DDT is given in Fig. 2. When the turbulent flame speed crosses a certain threshold, pressure begins to rise in the flow. This compresses and heats fuel, thereby further accelerating burning, which causes pressure to grow even more rapidly. As a result, a catastrophic runaway process is initiated leading to the formation of strong shock waves and, ultimately, to the detonation ignition.[3] The threshold burning velocity is known as the speed of the Chapman–Jouguet (CJ) deflagration. This is the theoretical maximum speed at which stable flame propagation is possible. Typical laminar chemical and thermonuclear flames have much lower burning velocities. Our simulations show, however, that turbulent flames can become sufficiently fast to exceed the CJ deflagration threshold. When they do, DDT occurs.[3]

Summary and Future Directions: Numerical simulations discussed here present the first self-consistent demonstration of spontaneous DDT in unconfined systems. A survey of different reactive mixtures and turbulent conditions showed that the obtained DDT criterion based on the CJ deflagration speed indeed very accurately predicts the onset of DDT.[3]

Large-scale simulations of combustion systems, such as SNIa or industrial explosions, however, can-

not resolve all scales of burning and, thus, must be supplemented with subgrid-scale models, which specify the local turbulent flame speed based on the resolved turbulent conditions. Existing subgrid-scale models do not account for unsteady phenomena such as DDT. Therefore, the next step in this work involves the incorporation of the CJ-based DDT criterion into the subgrid-scale models for the turbulent flame speed, suitable for use in large-scale simulations.

A preliminary subgrid-scale model developed for SNIa predicts that DDT will occur in these systems at densities ~10^7 g/cm^3. Occurrence of DDT at this density was previously empirically shown to give the best agreement with the observations, which demonstrates the viability of the emerging understanding of the unconfined DDT in realistic combustion systems.

[Sponsored by AFOSR and the NRL Base Program (CNR funded)]

References

[1] A.Y. Poludnenko and E.S. Oran, "The Interaction of High-Speed Turbulence with Flames: Global Properties and Internal Flame Structure," *Combustion and Flame* **157**, 995 (2010).

[2] A.Y. Poludnenko and E.S. Oran, "The Interaction of High-Speed Turbulence with Flames: Turbulent Flame Speed," *Combustion and Flame* **158**, 301 (2011).

[3] A.Y. Poludnenko, T.A. Gardiner, and E.S. Oran, "Spontaneous Transition of Turbulent Flames to Detonations in Unconfined Media," *Physical Review Letters* **107**, 054501 (2011).

Failure of Classical Elasticity

C.M. Roland, J. Roh, and P. Mott
Chemistry Division

Introduction: Determining the mechanical properties of very hard materials, such as diamond or beryllium, can be challenging. Usually, measurements of the sound velocity or Brillouin scattering are used to quantify certain elastic properties. Since there are only two unique constants for an isotropic material, the elastic constants of interest can then be calculated using the equations of "classical elasticity" (i.e., linear elasticity theory). Of course, the accuracy of such determinations depends on the validity of the classical equations.

An important elastic constant is Poisson's ratio, ν, defined as the negative ratio of the lateral strain ε_{22} to the longitudinal strain ε_{11}. Poisson's ratio can be used to determine the limits of applicability of the classical theory. From the equation relating ν to the bulk, B, and shear, G, moduli,

$$G = B\frac{3(1-2\nu)}{2(1+\nu)}, \qquad (1)$$

and the equilibrium requirement that B and G are both greater than zero, the bounds on Poisson's ratio for an isotropic material are obtained:

$$-1 < \nu < \tfrac{1}{2}. \qquad (2)$$

These well-known limits can be found in engineering texts dating from the 19th century.[1] (Sometimes a less than or equal sign is given erroneously for the upper bound in Eq. (2).[2])

Deriving the limits for ν based on B and G is the obvious approach, since these moduli describe the respective changes in a body's size and shape. However, there is neither mathematical nor physical justification for choosing B and G over other pairs of elastic constants. Recently we showed[3] that expressions derived for ν in terms of Young's modulus, the longitudinal modulus, the biaxial modulus, etc. lead to a different lower limit on ν than Eq. (2). From our analysis we concluded that classical elasticity can only be applied to materials for which

$$\tfrac{1}{5} \le \nu < \tfrac{1}{2}. \qquad (3)$$

Since all elastic constants are equally valid, the most restrictive bounds are the correct ones, since they are consistent with any less restrictive limits. Equation (3) also has the appealing feature that it coheres with the range of ν observed for more than 99% of materials. However, it is the few substances for which $\nu < 1/5$ that are of particular interest, because those are the cases for which the (inapplicable) classical elasticity equations are usually employed.

Results: Although the mathematics leading to Eq. (3) is straightforward, ideas long venerated are difficult to overturn. Remarkably, the classical bounds (Eq. (2)) have never been subjected to experimental verification. Thus, we carried out experiments[4] to validate our finding that classical elasticity fails whenever $\nu < 1/5$. Four samples were prepared (Table 1): a polyurethane foam (PU1) and a solid elastomer (polyisoprene), which had respective values of Poisson's ratio at each extreme of the range in Eq. (3), and two foams (PU2 and PU3) for which $\nu < 0$. These two auxetic samples enable testing of our prediction that classical elasticity fails for $\nu < 1/5$ (Fig. 3).

For each sample, ν, G, and Young's modulus, E, were measured at a strain rate of 0.002 s^{-1}, which is sufficiently slow to yield elastic (mechanical equilibrium) values. The Poisson's ratio of the samples was also calculated using the equation from classical elasticity:

$$\nu_{calc} = \frac{E}{2G} - 1. \qquad (4)$$

The calculated and experimental values of ν are compared in Fig. 4; the results extrapolated to zero strain

TABLE 1 — Poisson's Ratios

	polyisoprene	PU1	PU2	PU3
$\nu_{calc}\ \gamma = 0$	0.499 ± 0.014	0.206 ± 0.012	–0.590 ± 0.020	–0.608 ± 0.023
ν_{exp}	0.496 ± 0.006	0.204 ± 0.006	–0.699 ± 0.008	–0.650 ± 0.015

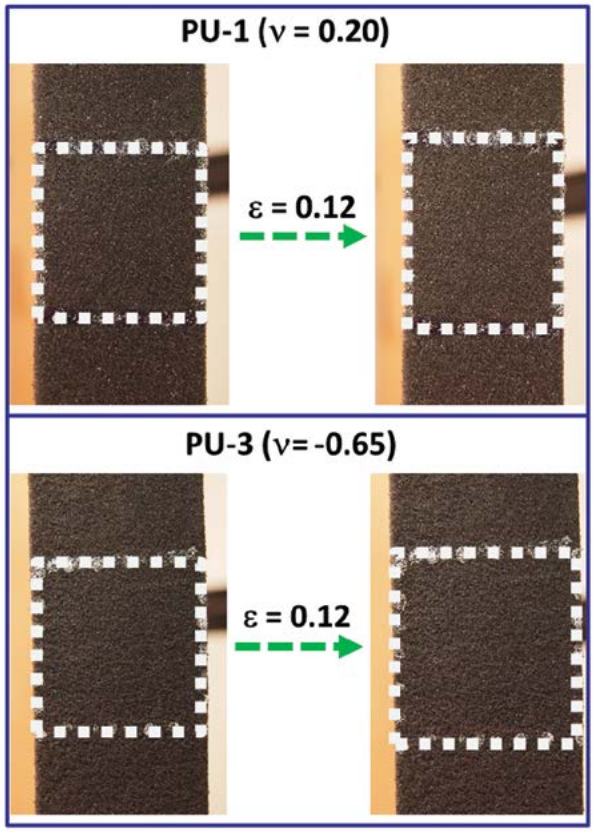

FIGURE 3
Photographs of polyurethane foams; the square markers represent fiducial marks used to calculate strains. Top: Conventional foam exhibiting lateral contraction upon stretching, in accord with a positive Poisson's ratio. Bottom: Auxetic foam, in which de-buckling of the cell structures compensates for the material contraction, yielding lateral expansion upon axial stretching.

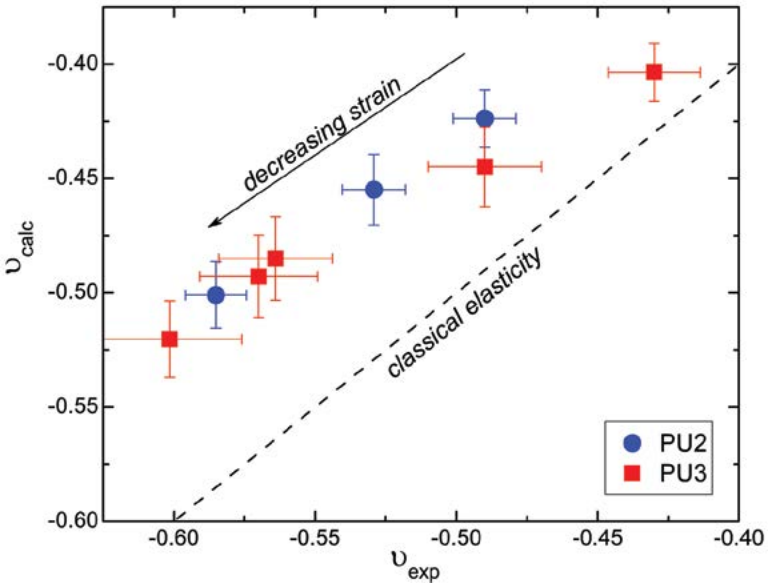

FIGURE 4
The values of Poisson's ratio calculated using Eq. (4) versus the measured *v* for the auxetic foams. Extrapolation to zero strain does not yield convergence.

are listed in Table 1. For the two materials with $\nu \geq 0.2$, Eq. (4) is accurate. However, for the two materials with $\nu < 1/5$ (within the traditional limits of Eq. (2), but beyond the more restrictive range), the calculated values ν are significantly larger than the measured values. Thus, Eq. (4) of classical elasticity fails when $\nu < 1/5$.

Summary: A recent derivation[3] of the bounds on Poisson's ratio, ν, for linearly elastic materials showed that the equations of classical elasticity are invalid for ν less than 1/5; that is, the lower bound for the classical theory is not −1, as commonly assumed. To verify this analysis, Poisson's ratio was measured for four materials. Two of these comply with the stricter limits for Poisson's ratio, and their calculated and measured values of ν were in agreement. However, for the two isotropic, auxetic foams, having ν outside the lower bound of Eq. (3), the values calculated using classical elasticity were significantly different than the measured ν. These results[4] corroborate our determination of the correct limits on ν for the classical theory to be applicable.

The significance of this work is that the small number of materials having $\nu < 0.2$ tend to be very hard, which makes direct measurement of Poisson's ratio and other elastic constants difficult and associated with large error. It is for this reason that recourse is made to the equations of classical elasticity. Unfortunately, this is the situation, as shown herein, for which the classical equations are invalid.

Acknowledgments: We thank C.B. Giller for experimental assistance.

[Sponsored by the NRL Base Program (CNR funded)]

References

[1] A.E.H. Love, *A Treatise on the Mathematical Theory of Elasticity*, Vol. 1 (Cambridge University Press, 1892).

[2] P.H. Mott, J.R. Dorgan, and C.M. Roland, "The Bulk Modulus and Poisson's Ratio of 'Incompressible' Materials," *J. Sound Vibration* **312**, 572–575 (2008).

[3] P.H. Mott and C.M. Roland, "Limits to Poisson's Ratio in Isotropic Materials," *Physical Review B* **80**, 132104 (2009).

[4] J.H. Roh, C.B. Giller, P.H. Mott, and C.M. Roland, "Failure of Classical Elasticity in Auxetic Foams," *AIP Advances*, submitted (2013).

♦

Synfuel from Seawater

H.D. Willauer,[1] D.M. Drab,[2] F. DiMascio,[3] D.R. Hardy,[4] R. Ananth,[5] and F.W. Williams[5]

[1]*Materials Science and Technology Division*
[2]*National Research Council Postdoctoral Associate*
[3]*Office of Naval Research*
[4]*Nova Research, Inc.*
[5]*Chemistry Division*

Introduction: NRL is developing and demonstrating technologies that recover carbon dioxide (CO_2) and produce hydrogen (H_2) from seawater. These feedstocks are combined in an NRL gas-to-liquid (GTL) process to produce hydrocarbons, which can be used to produce fuel at sea.

Synthesizing drop-in replacements for petroleum-derived fuel in-theater is a "game-changing" proposition for the Navy. Refueling U.S. military vessels with petroleum-derived fuel, at sea and underway, is a costly endeavor in terms of logistical tails, time, and decreased operational flexibility. In addition, refueling vessels at sea is risky, as ships must remain in close proximity and match course and speed for hours. Producing fuel at sea, from the sea, reduces these vulnerabilities and reduces dependence on fossil fuels. From an environmental perspective, this combination of integrated processes could be considered CO_2 neutral: the carbon dioxide produced from combustion of the synthetic fuel is returned to the atmosphere where it re-equilibrates with the ocean to complete the natural carbon cycle.

Carbon Capture: Using a novel electrochemical acidification cell developed at NRL, up to 92% of both dissolved and bound CO_2 can be removed from seawater. The concentration of carbon dioxide in seawater is 140 times greater than that in air, yet harvesting large quantities of CO_2 rapidly and efficiently from seawater had not been demonstrated prior to the recently announced, patented NRL process.[1] In addition to recovering CO_2, the cell simultaneously produces H_2 gas at the cathode as a byproduct. NRL and partners have developed a carbon capture skid, shown in Fig. 5, that demonstrates the continuous and efficient production of CO_2 and H_2 from seawater. The process of both recovering CO_2 and concurrently producing H_2 gas eliminates the need for additional large and expensive electrolysis units. The process efficiency, H_2 production, and ability to process the seawater without the need for additional chemicals or pollutants have made this technology far superior to membrane and anion exchange processes previously developed and tested by NRL for use at sea.

Synfuel Production: Achieving high catalytic conversion efficiencies and selectivities of CO_2 and H_2 to a jet fuel fraction is a key scientific challenge which NRL continues to study at the basic science level. [2] NRL has made significant advances in the development of a two-step GTL process to convert CO_2 and H_2 from seawater to a fuel-like fraction of C_9–C_{16} molecules. In the first step (Fig. 6), an iron-based catalyst has been developed that can achieve CO_2 conversion levels up to 60% and decrease unwanted methane production from 97% to 23% in favor of longer-chain unsaturated hydrocarbons (olefins). In the second step, by a second solid acid catalyst reaction, these olefins can be oligomerized (a chemical process that converts monomers, molecules of low molecular weight, to a compound of higher molecular weight by a finite degree of polymerization) into liquid containing hydrocarbon molecules in the C_9–C_{16} range, suitable for conversion to jet fuel.[2] NRL operates a laboratory-scale fixed-bed catalytic reactor system, and the outputs of this prototype unit have confirmed the presence of the C_9–C_{16} molecules in the liquid fuel.

FIGURE 5
NRL electrochemical acidification carbon capture skid. The acidification cell is mounted onto a portable skid along with a reverse osmosis unit, power supply, pump, carbon dioxide recovery system, and hydrogen stripper to form a carbon capture system (dimensions 63 in. × 36 in. × 60 in.).

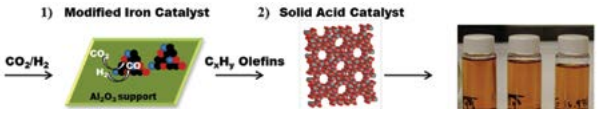

FIGURE 6
NRL liquid hydrocarbons synthesized from carbon dioxide and hydrogen.

The Future of Synfuel at Sea: We are now set to transition the NRL two-step GTL process into commercial modular reactor systems of the type being designed for other offshore and remote synthetic hydrocarbon fuel synthesis from syngas. The new challenge is to continue optimizing the chemistry of the two-step approach in a commercial system, so that this data can provide the basis for future modular pilot- and commercial-scale processes.

[Sponsored by the NRL Base Program (CNR funded)]

References

[1] H.D. Willauer, F. DiMascio, D.R. Hardy, M.K. Lewis, and F.W. Williams, "Development of an Electrochemical Acidification Cell for the Recovery of CO_2 and H_2 from Seawater II. Evaluation of the Cell by Natural Seawater," *I&EC Res.* **51**(34), 11254-11260 (2012).

[2] D.M. Drab, H.D. Willauer, M.T. Olsen, R. Ananth, G.W. Mushrush, J.W. Baldwin, D.R. Hardy, and F.W. Williams, "Hydrocarbon Synthesis from Carbon Dioxide and Hydrogen: A Two-step Process," *Energy Fuels*, DOI: 10.1021/ef4011115 (2013).

♦

Relationship of Grain Boundary Microchemistry to Stress Corrosion Susceptibility in Aircraft Aluminum Alloys

R. Goswami, P.S. Pao, and R.L. Holtz
Materials Science and Technology Division

Introduction: Aluminum 7000 series alloys are used extensively for military and civilian aircraft structural components. However, stress corrosion cracking (SCC) of the higher strength tempers in salt spray/salt fog environments continues to be a problem with these alloys, particularly with respect to maintenance costs. In salt water environments, SCC susceptibility is the result of anodic dissolution of grain boundary precipitates. Certain aging, or precipitation hardening, treatments can improve the resistance to SCC of the 7000 aluminum alloys, and increasing the copper content of the alloy can reduce the dissolution rate of the grain boundary precipitates in corrosive environments. To better understand this behavior and the factors that control SCC, NRL has undertaken a systematic investigation of the effects of aging/hardening treatments and Cu content on the microchemistry and microstructure of grain boundary precipitates of 7075Al alloy.

Grain Boundary Precipitate Structure and Microchemistry: The microstructure evolution of grain boundary precipitates as a function of aging is demonstrated by Fig. 7. Table 2 defines the aging treatments. In naturally aged (NA) condition (Fig. 7(a,b)), grain boundaries are observed to be decorated by nanocrystalline precipitates 5 to 10 nm in size. Extremely fine precipitates (Fig. 7(b,c)), mostly Zn-rich GP zones, can be observed within the grain. At peak-aged (PA)

condition, the precipitates at grain boundaries are much coarser, 50 to 100 nm (Fig. 7(d)). Upon further aging (over-aged condition, OA), the size and spacing of the precipitates (Fig. 7(e)) increase to some extent as compared to the peak-aged condition. Transmission electron microscope (TEM) studies showed that the grain boundary precipitates are η phase ($MgZn_2$) containing considerable amounts of Cu.

TABLE 2 — Aging Treatment Definitions

Aging Designation	Alloy Hardening Treatment
Naturally aged	Allowed to harden at room temperature
Peak-aged (T651 condition)	Reheated to an intermediate temperature
Over-aged (T73 condition)	Reheated to a higher temperature beyond peak strength

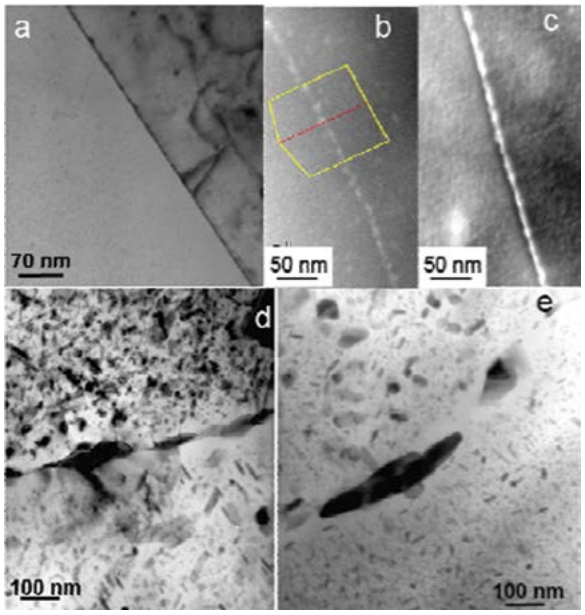

FIGURE 7
Microstructure of grain boundary precipitates in samples with different aging treatments. (a) Bright-field TEM image showing grain boundary precipitates in the naturally aged condition. (b) HADDF image of the naturally aged condition. (c) HAADF image of a sample aged at 120 °C for 12 h (less aging than peak-aged). (d) Bright-field TEM image at peak-aged condition. (e) Bright-field TEM image at over-aged condition.

Figure 8(a) shows grain boundary precipitates in a peak-aged sample. Figure 8(b) is a high-resolution TEM (HRTEM) image of one such grain boundary precipitate close to the [0001] zone. The fast Fourier transform (FFT) obtained from this precipitate showed {10-10} type spots with d-spacing ~4.5 Å. Composition maps of Mg, Al, Cu, and Zn and corresponding high-angle annular dark field (HAADF) images were obtained for the different aging conditions; those of the peak-aged condition are shown in Fig. 8(c,d). The composition of precipitate as a function of aging is given in Fig. 9(a), showing a significant increase in Cu content with aging; the Zn decreases considerably and the Mg increases by a small amount (compared to the naturally aged condition). At peak-aged condition, the average content of Mg, Cu, and Zn is 45.18, 15.08, and 39.73 at.%, respectively, and at over-aged condition, the average content of Mg, Cu, and Zn is 40.0, 20.00, and 40.00 at.%, respectively.[1] The precipitate stoichiometry is close to $Mg(Cu_xZn_{1-x})_2$.

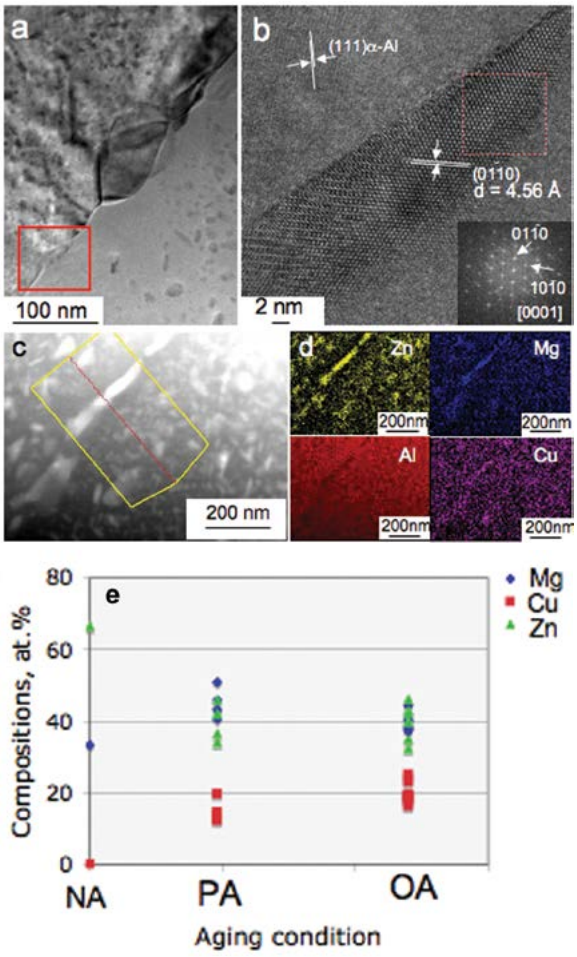

FIGURE 8
(a) Bright-field TEM image at peak-aged condition showing a grain boundary with several precipitates. (b) HRTEM image of one such precipitate showing the crystal structure of the precipitate conforms to hexagonal $MgZn_2$. (c) HAADF image of a grain boundary precipitate in a peak-aged sample. (d) Elemental maps of Mg, Al, Cu, and Zn. (e) The average composition of Zn, Mg, and Cu of the grain boundary precipitate as a function of aging conditions: naturally aged (NA), peak-aged (PA), and over-aged (OA).

Grain Boundary Precipitate Dissolution Behavior: To study the dissolution behavior of the η phase, TEM samples were immersed for 180 to 300 seconds in a brine solution containing 3.5% NaCl at room temperature; subsequent TEM observations were then carried out. For the naturally aged samples, it was observed that grain boundaries were completely dissolved after 300 seconds in the salt water (see Fig. 9(a,b)). However, in peak-aged samples, the precipitates at the grain boundary did not dissolve completely for the same immersion duration (Fig. 9(c)). Our compositional analyses showed that the Cu content of the η phase in the peak-aged condition is 15 at.%, considerably higher than in the naturally aged condition, where it is negligible. The dissolution rate can be directly correlated with the electrochemical potential of the $Mg(Cu_xZn_{1-x})_2$ compound, which has been observed to increase with an increase in Cu content. This increase in electrochemical potential decreases the driving force for anodic dissolution with respect to the matrix with aging, which suggests the rate of dissolution decreases with the increase in Cu content.

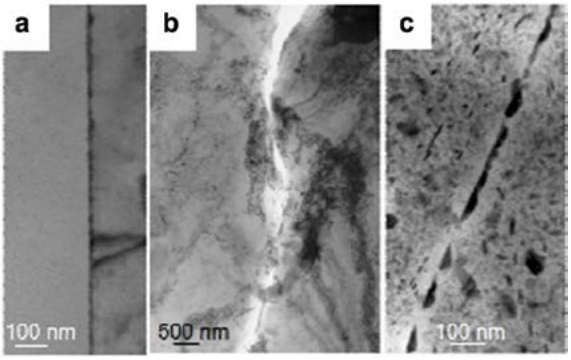

FIGURE 9
(a) Typical grain boundary precipitates in the naturally aged condition before immersion in salt water. (b) Grain boundaries showing the complete dissolution of precipitates in a naturally aged sample after 300 seconds exposure to salt water. (c) Grain boundary in a peak-aged sample showing the precipitates after 300 seconds exposure to salt water.

Significance: An increase in Cu content of the grain boundary precipitates in 7075 alloy was observed for peak-aged and over-aged conditions, relative to the naturally aged condition, in which the Cu content is negligible. The observed increase in Cu content of the precipitates with aging correlates with the increasing resistance to intergranular stress corrosion cracking. The electrochemical potential of the intermetallic $Mg(Cu_xZn_{1-x})_2$ compound increases with the increase in Cu content. This decreases the driving force for anodic dissolution with respect to the matrix, particularly for the over-aged condition, in which the Cu level is highest. As the dissolution rate decreases with increasing Cu content, the alloy becomes less susceptible to SCC. This result is significant to the Navy in that it demonstrates that Cu enrichment of grain boundary precipitates increases the resistance to crack growth in salt water environments.

[Sponsored by ONR]

Reference

[1] R. Goswami, S. Lynch, N.J.H. Holroyd, S.P. Knight, and R.L. Holtz, "Evolution of Grain Boundary Precipitates in Al 7075 Upon Aging and Correlation with Stress Corrosion Cracking Behavior," *Metallurgical and Materials Transactions* **44A**, 1268–1278 (2012), doi:10.1007/s11661-012-1413-0.

A New Annealing Technique: Multicycle Rapid Thermal Annealing (MRTA)

B.N. Feigelson, T.J. Anderson, J.A. Freitas, J.K. Hite, C.R. Eddy, Jr., and F.J. Kub
Electronics Science and Technology Division

Problem: Ion implantation is required for selective-area doping of gallium nitride (GaN) to enable advanced high-power devices.[1] Therefore, post-implant damage removal and impurity activation are critical steps to achieve high quality GaN crystals with high mobility and high dopant activation. To date, there has been no reliable method for annealing Mg-implanted p-GaN to result in adequate Mg electrical activation. The main hurdle for the annealing is the dissociation of GaN at temperatures above 850 °C at atmospheric pressure. Equilibrium nitrogen pressure above GaN increases quickly with temperature, and exceeds 0.1 MPa (1 bar) at 850 °C (only one-third of the melting point). At the same time, it is known that estimated annealing temperature required for sufficient diffusion is about two-thirds of the melting point of the material, and for GaN it is about 1400 to 1500 °C.[2]

Solution: Annealing at high N_2 pressure (HP) allows the heating of GaN to high temperatures for a long time without GaN dissociation, but the use of very high gas pressures (>2.0 GPa) requires unique HP equipment and time-consuming procedures to load samples and to apply high N_2 pressure. This makes HP annealing too expensive for industry and difficult to scale up to larger wafer sizes. Rapid thermal annealing (RTA) with a protective cap is an attractive alternative for GaN annealing in terms of achievable temperatures and costs, but no electrical activation of Mg after the implantation in GaN without co-doping with other

ions has been shown yet.[3] One probable reason for these unsuccessful attempts is the short duration of the GaN annealing at high temperatures. A new technique is required to enable a long-duration annealing at high temperatures without GaN decomposition.

The proposed and developed technique is described as follows. First, consider the case in which a GaN layer with a protective cap is annealed for a very short time at a temperature far above GaN thermodynamic stability. With a careful choice of the cap material and heating duration, it is possible to avoid decomposition of the GaN under the cap. After cooling the sample, the same heating procedure can be repeated without deteriorating the GaN. Following this logic, it should be possible to anneal GaN many times while maintaining the stability of the surface if the heating time above the stability range is sufficiently short and the cap is sufficiently robust. Finally, if this process is repeated without cooling to room temperature, instead just cooling to a temperature where GaN returns to thermodynamic stability, it is possible to rapidly cycle this annealing procedure. In such a process, the material is exposed to high temperature above GaN thermodynamic stability for a long time by accumulating the time of each repetitive cycle, but the stability is maintained due to the extremely short heating duration of each single cycle. Such a process has been developed at NRL, and is described as multicycle rapid thermal annealing (MRTA).[4]

Experimental Details and Results: The GaN films used in the study were grown in a Thomas Swan metal organic chemical vapor deposition (MOCVD) reactor on sapphire substrates. The samples consisted of a 25 nm thick, low-temperature (700 °C) aluminum nitride (AlN) buffer layer, a 2 μm thick, unintentionally doped GaN layer (1030 °C), followed by a thin AlN capping layer. The AlN cap was 4 nm thick, grown at 1000 °C, which was intended to protect the GaN surface during annealing. A single growth run was used to deposit all three layers.

Implantation of only Mg ions was performed to validate the new annealing technique itself. The Mg implant profile was calculated using TRIM implant simulation software.

All annealing experiments were conducted in a chamber with a nitrogen overpressure of 2.0 MPa. A radio-frequency (RF) generator with a graphite susceptor is used for heating. Prior to MRTA, the samples were conventionally annealed in the same chamber for 1 h at 950 to 1050 °C. A typical MRTA schedule is shown in Fig. 10.

The evident advantage of MRTA is clearly shown in the micrographs of Fig. 11. The sample did not show signs of surface degradation after one cycle of the rapid annealing when total heating time between 1300 and 1400 °C was less than 23 s (Fig. 11(a)), but drops of Ga, as a result of GaN dissociation, were seen on the surface of the sample when this time exceeded 31 s (Fig. 11(b)). However, the surface of the sample maintained continuity, i.e., no cracking or GaN decomposition, after MRTA of 40 cycles with the cumulative time between 1300 and 1400 °C totaling 5 min 34 s (Fig. 11(c)).

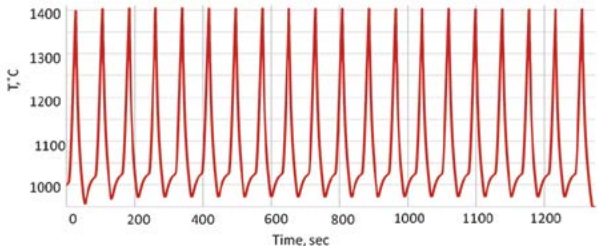

(a)

Run	Accumulated time			Cycles
	From	To	Time	
	T_1°C	T_2°C	min:sec	
CZ108	1300	1405	3:05	20
CZ113	1300	1410	2:59	20
CZ114	1300	1415	5:34	40

(b)

FIGURE 10
(a) Typical MRTA schedule; (b) MRTA accumulates large total time at high temperature and maintains the stability of the material due to the short duration of each single cycle.

Electrical measurements were performed to look for evidence of Mg activation. It was found that an undoped and unimplanted reference sample was highly resistive (500 MΩ/□), while there was a few orders of magnitude decrease in sheet resistance measured by the transmission line method (TLM) in the implanted and MRTA annealed samples. Hall measurements confirmed the sheet resistance value, and for the first time verified p-type conductivity in Mg-implanted GaN (Fig. 12).

Summary: A new annealing technique, designated multicycle rapid thermal annealing, or MRTA, has been developed to enable annealing of GaN layers. The technique has been proven by the demonstration of electrically active acceptors after Mg implantation in GaN, and for the first time, p-type conductivity in Mg-implanted samples without co-doping enhancement has been observed. Annealing of other nonstable materials may also benefit by applying the MRTA method.

[Sponsored by the NRL Base Program (CNR funded)]

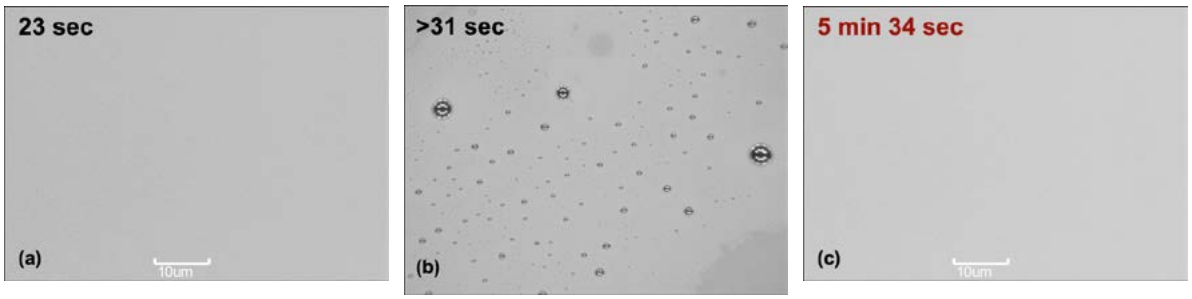

FIGURE 11
Optical micrographs of the annealed samples: (a) one cycle with 23 s total heating time between 1300 and 1400 °C; (b) one cycle with 45 s total heating time between 1300 and 1400 °C; (c) MRTA 40 cycles with 5 min 34 s total cumulative heating time between 1300 and 1400 °C.

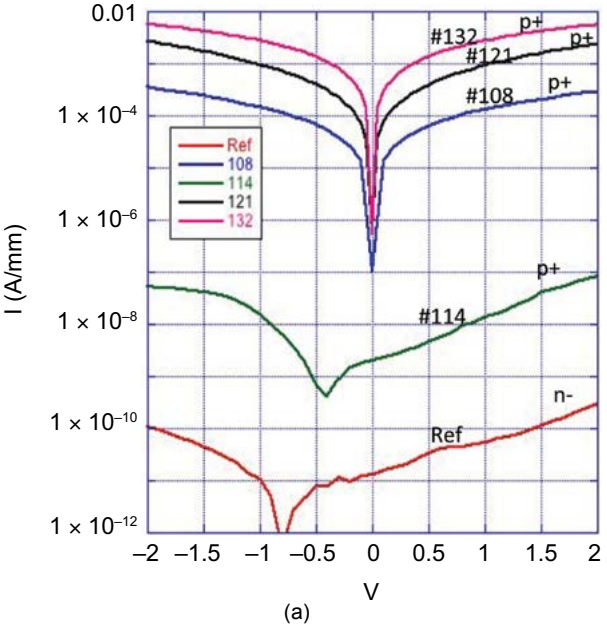

(a)

Sample #	R_{SH} kΩ/□	μ $cm^2/V•s$	N_A (cm^{-3})	Activation %
108	42.6	5	$8.4×10^{17}$	1.4
114	4850	1	$3.7×10^{15}$	<0.1
121	5.38	20	$1.7×10^{18}$	8.2
132	2.69	40	$1.7×10^{18}$	8.2

(b)

FIGURE 12
(a) I–V curves for a reference sample (as-grown GaN sample, which is unintentionally doped and exhibits n-type conductivity) and Mg-implanted MRTA annealed samples; (b) sheet resistance (R_{SH}), mobility (μ), concentration of noncompensated acceptors (N_A), and activation % of all annealed samples.

References

[1] K.T. Liu, S.J. Chang, S. Wu, and Y. Horikoshi, "Crystal Polarity Effects on Magnesium Implantation into GaN Layer," *Japanese Journal of Applied Physics* **49**(7), 071001 (2010).

[2] S.J. Pearton, "Ion Implantation in Group III Nitrides," in *Comprehensive Semiconductor Science and Technology*, Vol. 4, pp. 25–43 (Elsevier, Amsterdam, 2011).

[3] K.T. Liu, Y.K. Su, S.J. Chang, and Y. Horikoshi, "Magnesium/nitrogen and Beryllium/nitrogen Coimplantation into GaN," *Journal of Applied Physics* **98**(7), 073702 (2005).

[4] B.N. Feigelson, T.J. Anderson, M. Abraham, J.A. Freitas, J.K. Hite, C.R. Eddy, and F.J. Kub, "Multicycle Rapid Thermal Annealing Technique and its Application for the Electrical Activation of Mg Implanted in GaN," *Journal of Crystal Growth* **350**, 21–26 (2012).